AMERICAN
METEOROLOGICAL
SOCIETY

Journal of Climate

The DOI for this manuscript is doi: 10.1175/2008JCLI2078.1

Sensitivity of MJO simulation and predictability to sea surface temperature variability

Hye-Mi Kim[1], Carlos D. Hoyos[2], Peter J. Webster[2], and In-Sik Kang[1]

[1]*School of Earth and Environmental Science, Seoul National University, Seoul, Korea*

[2]*School of Earth and Atmospheric Sciences, Georgia Institute of Technology, Atlanta, Georgia*

May, 2007

Submitted to *J. Climate*

(Submitted with Revisions January 2008)

Corresponding author address: Hye-Mi Kim, School of Earth and Environmental Sciences, Seoul National University, Seoul, 151-742, Korea

E-mail: hmkim@climate.snu.ac.kr

Tel. : +82-2-880-8124

Fax : +82-2-885-7357

Abstract

The influence of sea surface temperature (SST) on the simulation and predictability of Madden-Julian Oscillation (MJO) is examined using the Seoul National University atmosphere general circulation model (SNU AGCM). Forecast skill was examined using serial climate simulations spanning eight different winter seasons with 30-day forecasts commencing every 5 days giving a total of 184 30-day simulations. The serial runs were repeated using prescribing observed SST with monthly, weekly and daily temporal resolutions. The mean SST was the same for all cases so that differences between experiments results from the different temporal resolutions of the SST boundary forcing.

It is shown that high temporal SST frequency acts to improve 1) the MJO activity of 200 hPa velocity potential field over the entire Asian-monsoon region at all lead-times; 2) the percentage of filtered variance of the two leading EOF modes that explain the eastward propagation of MJO; 3) the power of the wavenumber one eastward propagating mode; and 4) the forecast skill of MJO, maintaining it for longer periods. However, the MJO phase relationship between MJO convection and SST, as is often the case with many atmosphere-only models, although well-simulated at the beginning of forecast period, becomes distorted rapidly as the forecast lead time increases, even with the daily SST forcing case. Comparison of AGCM simulations with coupled GCM integrations shows that ocean-atmosphere coupling improves considerably the phase relationship between SST and convection. The CGCM results reinforce that the MJO is a coupled phenomena and suggests strongly the need of the ocean-atmosphere coupled processes to extend predictability.

1. Introduction

The low-frequency intraseasonal oscillation (ISO) is a dominant mode of tropical variability accounting for a large percentage of variance of convection (e.g Zhang 2005). The mode possesses a distinct seasonal character. During the Northern Hemisphere winter and springtime, the ISO, often referred to as Madden-Julian Oscillation (MJO; Madden and Julian 1994), is associated with strong convection that originates in the Indian Ocean and moves eastward across the Pacific with a periodicity of about 30-70 days. During the Northern Hemisphere summer, there is a pronounced northward propagation of ISO from the equatorial Indian Ocean and into South and Southeast Asia introducing high amplitude modulations of the Asian summer monsoon (e.g., Webster et al. 1998, Hoyos and Webster 2007). The MJO/ISO explains a large fraction of the overall tropical intraseasonal variability and in some regions of the tropics its amplitude is even larger than the annual cycle (e.g., the equatorial Indian Ocean: Hoyos and Webster 2007). The MJO/ISO is particularly important because of its dominant influence on monsoon dynamics, generating active and break phases of convection during the South-East Asian and Australian monsoons (Yasunari 1979, Lau and Chan 1986, Kang et al. 1989, Webster et al, 1998, Kang et al. 1999, Lawrence and Webster 2002, Hoyos and Webster 2007) and on general weather and climate variability (Ferranti et al. 1990, Jones et al. 2004). Overall, the ISO has a large impact on global medium and extended range forecast skill (Chen and Alpert 1990, Hendon et al. 2000, Jones and Schemm 2000, Webster and Hoyos 2004). In addition, there is evidence that ISOs play an important role in initiating El Niño events (e.g. Bergman et al. 2001).

In spite of efforts during the last decade in developing more representative models of the climate system and increasing the basic understanding of the MJO/ISO phenomenon, the ability to simulate and predict intraseasonal variability by state-of-the-art general circulation models (GCMs) has not increased accordingly (Slingo et al. 1996, Kang et al. 2002, Waliser et al. 2003, Lin et al. 2005, Sperber et al. 2005, Zhang 2005, Kim et al. 2007). Very few models reproduce accurately the fundamental features of the MJO/ISO such as the general eastward propagation through the tropics or its northward excursion into South Asia during the summer. Furthermore, most GCMs do not estimate the magnitude of the MJO/ISO correctly and fail to maintain its strength compared to observations during extended integrations (Waliser et al. 2003, Kim et al. 2007).

Recent observational and modeling studies suggest that ocean-atmosphere coupling is important for the maintenance of MJO/ISO and also improve the simulation of MJO/ISO in terms of their intensity, propagation, seasonality, and predictability (Wang and Xie 1998, Waliser et al. 1999, Woolnough et al. 2000, Kemball-Cook et al. 2002, Webster et al. 2002, Fu et al. 2003, Inness and Slingo 2003, Fu and Wang 2004, Zheng et al. 2004, Wang et al. 2005, Agudelo et al. 2006, Fu et al. 2007). These studies suggest that the intraseasonal variability of the underlying sea surface temperature (SST) plays a determining role in the evolution and maintenance of the MJO/ISO.

Previous studies have shown that the SST has a significant spectral peak in the intraseasonal band (e.g. Hendon and Glick 1997) and that this SST band organizes a significant atmospheric response in numerical models that is more consistent with the observed MJO (Woolnough et al. 2001). Moreover, the use of SSTs that contain such an intraseasonal variability in atmospheric GCMs have been shown to improve the simulation of the MJO in comparison to the use of climatological mean SST fields. For example, Reichler and Roads (2005) showed that a model forced with weekly SST exhibits a more realistic MJO than models forced with SST climatology in terms of scale of variability, spectral power, and eastward propagating characteristics. Furthermore, the inclusion of intraseasonal SST variability appears to increase predictability (Reichler and Roads 2005). Although there is agreement on the importance of intraseasonal variability of SST in increasing the simulation and prediction of intraseasonal variability, there are also a number of problems introduced by methods to include the variability. A full coupling of ocean-atmosphere interaction, for example, often degrades both the simulated atmospheric and SST mean states. Systematic biases in these mean states, in turn, affect the model's capability to represent intraseasonal variability although the reduction of systematic error by flux adjustment significantly improved the simulation of intraseasonal variability in coupled simulations (e.g., Inness et al. 2003, Seo et al. 2007).

A major purpose of this study is to isolate the impact of intraseasonal SST variability on the MJO simulation. However, the magnitude and phase of mean SST state needs to be retained and the influence of a possible biased mean state minimized by examining the atmospheric response to realistic and accurate observed SST anomalies. To accomplish this, we conduct simulations using an atmospheric-only model by prescribing observed SST with different temporal resolution (monthly to 3-day SST) but where the mean state of SST is the same in each of the simulations. Then, from these experiments will emerge differences due to the temporal resolution of the subseasonal SST forcing. In this manner, the impact of intraseasonal SST variability is investigated on both the capability of a model to simulate the MJO, but also on the potential predictability of MJO assuming perfectly prescribed boundary conditions. The model used in the numerical experiment is the Seoul National University Atmospheric GCM (SNU AGCM, Kim et al. 1998).

To examine the predictability of MJO during the boreal winter with the GCM, we have developed a climate version of the Dynamical Extended Range Forecast (DERF) experiment (Tracton et al. 1989, Reynolds et al. 1994). A DERF experiment aims at examining changes in predictability in time and consists of a series of experiments run out to a specific horizon (the original DERF experiment consisted of 10-day forecasts) that are reinitialized and repeated for a specific period. Here, the GCM is initialized every 5 days and run out for 30 days relative to SST boundary conditions discussed in section 2. This procedure is repeated for 8 years. The “climate-DERF” procedure allows the evolution of elements of the global system (here the MJO/ISO) to be examined successively relative to evolving initial conditions. Initialization of the model through different phases of MJO allows the detection of the stage within the prediction period where the model loses skill. DERF-like experiments have proved useful in assessing the forecast skill at all convective stages of the MJO (Chen and Alpert 1990, Lau and Chang 1992, Lo and Hendon 2000, Hoyos 2006, Agudelo et al. 2006, 2008, Woolnough et al. 2007). Most DERF experiments are limited in their evaluation of forecasts skill because of the length of the integrations. This problem is avoided in the present study by performing experiments with 8-year duration, specifically from 1998 through 2005. Furthermore, other DERF-like studies have used SST fields that have been damped to climatology from observed initial states (e.g., Schemm et al. 1996). Here, the experiment is repeated using different temporal resolutions of SST all of which have the same mean SST.

To summarize, we aim specifically at determining the quality of the predictions of the MJO/ISO through forecast integrations for the 8–year period. With the use of three different resolutions of SST as a boundary condition, as well as a DERF experiment technique, we aim to quantify the impact of boundary forcing at different temporal resolutions, not only on simulation aspects but also on predictability.

The experimental framework of the climate DERF experiment and the datasets used are presented in section 2. Results are presented in section 3. Section 4 provides a synthesis and perspective of the results

2. Experimental framework and data sources

The basic model used in study is the Seoul National University AGCM (SNU AGCM, Kim et al. 1998) with T42 horizontal resolution and 20 vertical levels. The major physical parameterizations used are the simplified Arakawa-Schubert scheme for the convection (Moorthi and Suarez 1992), the k-distribution scheme for radiation (Nakajima and Tanaka 1986), the land surface model by Bonan (1998), a non-local PBL/vertical diffusion scheme (Holtslag and Boville 1993), and an orographic gravity wave drag parameterization (McFarlane 1987). Kim et al. (1998) showed that the SNU AGCM simulates reasonably well both the climatological mean patterns of tropical circulation and the corresponding anomalies during El Nino.

For comparative purposes, a coupled ocean-atmosphere version of the SNU model is used. The CGCM uses the same AGCM with T42 triangular truncation. The ocean component is MOM2.2 Oceanic GCM developed by the Geophysical Fluid Dynamic Laboratory (GFDL). A mixed layer model (Noh and Kim 1999) is embedded into the ocean model. Details of the coupled model are described in Kug et al (2007).

The model is driven with prescribed SST fields. These boundary conditions are spatially averaged onto the GCM grid, and then temporally interpolated to daily values. Figure 1 shows examples of the monthly, weekly and 3-day mean SST fields averaged over the Indian Ocean (60˚-90˚E, 10˚S-5˚N) for the period 15 Jan. 2004 to 13 Feb. 2004. Most atmospheric GCMs use prescribed monthly mean SST for boundary forcing that are interpolated to daily timescales (open circle: Fig. 1). However, large differences can be noted at higher resolution such as weekly ("x": Fig. 1) or daily (closed circle: Fig. 1) timescales. The three SST resolutions shown in Figure 1 are the basis of the experimentation discussed in this study.

The monthly mean and weekly mean SST data come from the optimum interpolation SST version 2 (Reynolds et al. 2002, available at www.cdc.noaa.gov/cdc/data.noaa.oisst.v2.html). The 3-day averaged SST data correspond to retrievals from Tropical Rainfall Measuring Mission (TRMM) satellite Microwave Imager (TMI) measurements. The TMI data set corresponds to SST averaged over 3 days comprised of daily moving average including ascending and descending passes with spatial resolution of 0.25 degrees from 40˚S-40˚N. This data is available at www.ssmi.com/tmi/tmi_description.html. As well as having higher time resolution, the TMI SST dataset is appropriate to look at the variables in the presence of clouds because it is based on microwave retrievals that are virtually less attenuated by upper-level clouds. Thus we consider this data as a reliable measurement of SST variability during the entire life cycle of the MJO. In preparing the SST data, missing regions are filled with monthly mean SST values. The 8-year extent of the experiment is determined by the availability of the TMI SST. Hereafter, we will refer to the experiment using monthly mean SST as “CTRL”, the weekly mean SST experiment as “WSST”, and 3-day mean SST experiment as “DSST”.

Figure 2 shows a schematic of the climate DERF scheme designed for this study. Each experiment consists of a 30-day forecast initialized successively every 5 day (00Z) using the NCEP-NCAR reanalysis-2 as initial conditions (Kanamitsu et al. 2002). For example, a single forecast run starts at 6 Nov. 1998 and progresses for 30-days. The forecast is repeated starting on 11 Nov. 1998 for a further 30-day forecast, and so on, from 6 Nov. 1998 to 24 Feb. 1999, and similarly for all years between 1998/1999 and 2005/2006. In total, 184 30-day serial forecast runs were performed. Here, we focus on the Northern Hemisphere winter season when the MJO peaks in magnitude (e.g. Madden and Julian 1994, Hendon and Salby 1994). All forecasts in the 1998/99-2005/2006 period are compared with NCEP/NCAR reanalysis fields.

Anomalies are calculated by removing the 8-year climatology for each 30-day forecasts at each grid point. To remove interannual variability (including ENSO), the mean of each 30-day forecast segment is subtracted. Finally, to extract the intraseasonal variability, we need to design a filtering technique. Band-pass filtering is not ideal in this case because the forecast segment is 30-days in length, which is shorter than the time scale of MJO. This issue is solved by using a 9-day moving average in each of forecast segment to remove the high frequency variability. The days prior to the 30-day forecast are padded with four days of analyses before the 9-day moving average is applied.

The same procedure was applied to the observed fields to allow a fair comparison. The observed daily-averaged atmospheric circulation velocity potential anomaly at 200 hPa (hereafter VP200) is calculated using the NCEP-NCAR reanalysis-2 data. In addition, the daily mean outgoing long-wave radiation (OLR) from National Oceanic and Atmospheric Administration (NOAA) polar-orbiting satellites is used as a proxy for tropical convective activity (e.g., Lau and Chan 1986). All data were interpolated to a spatial resolution of 2.8125° x 2.8125° in order to match the model resolution.

3. Results

a. Mean MJO/ISO variability

MJO/ISO activity is measured by the standard deviation of intraseasonally filtered VP200 and calculated both for observations and simulated fields for each forecast lead time. Figure 3 shows the global distribution of MJO/ISO activity from observations and the 10-day forecast lead times of the three experiments. The largest amplitude of the observed MJO/ISO activity appears in the Indian Ocean-western Pacific sector. This pattern is reproduced well in all experiments although with weaker amplitudes. However, the magnitude of the MJO/ISO activity increases with the temporal resolution of the SST. The DSST (Fig. 3d) shows the strongest MJO/ISO activity among the three experiments, followed by the WSST and then CTRL, in amplitude-descending order.

To quantify the differences in MJO/ISO activity between the three experiments, the area averaged MJO/ISO activity is computed as a function of forecast day over the area

40˚E-180˚E and 30˚S-30˚N, which is a region of high MJO/ISO activity (Fig. 4). It is seen that the MJO/ISO activity decreases with the forecast lead time. The DSST (CTRL) shows the greatest (lowest) amplitude of MJO/ISO activity for all forecast lead-times. The weak magnitude of intraseasonally filtered upper level winds is one of the problematic features in several models (e.g. Wu et al. 2002, Seo et al. 2005). This weakening can perhaps be explained, in part, by the lack of intraseasonal SST variability in models. Thus, if higher frequency SST is resolved by models, the chance of representing higher amplitude MJO/ISO increases.

b. Dominant modes of MJO

An empirical orthogonal function (EOF) analysis was performed on the intraseasonally filtered VP200 fields for each forecast lead time in the tropical strip from 40˚S to 40˚N. The aim of this procedure is to determine the dominant modes of intraseasonal variability. Analysis of observations shows a dipole evident in the first EOF (42% of the filtered variance; Fig. 5a), with the centers of action located over the Indian Ocean and western Pacific and over the eastern Pacific. The second EOF (31% of the filtered variance; Fig. 5b) reveals a similar dipole but with the centers of action shifted eastward. The first two EOFs represent the well known eastward propagating pattern of the MJO with a quarter-cycle phase difference between the two principal components (e.g. Lorenc 1984). Because the pattern of the leading eigenvectors for each experiment is similar through all of the forecast times, we only show the EOF patterns for the 30-day forecast in CTRL, WSST and DSST, respectively (Fig.5c-h). Although there are slight differences in phase and magnitude, the leading observational modes are relatively well simulated in all of the experiments with similar centers of action.

Figure 6 shows the percentage of filtered variance captured by the first and the second leading EOFs from each of experiments. Though the eigenvectors of the forecast VP200 show very similar patterns compared to those obtained from observations (Fig. 5), there are differences in the percentage values in each of experiments as forecast time increases. Overall, the percentage of explained variance by the first two modes is considerably smaller throughout the entire forecast than the 72% determined from observations. At the beginning of the forecasts, the explained variance by the leading modes is high at about 68%, however, as the lead time increases the amplitude decreases rapidly in all three experiments. It is important to note, though, that the DSST always possesses the largest value of the three experiments and it is never less than 50% except for the last few days of the 30-day forecasts. These results indicate that, in spite of the similar spatial structure of the eigenvectors in all three experiments, the leading modes are most similar to the observed MJO mode when it is forced with higher temporal resolution of SST.

The high correlation between the two principal components (PCs) around the 10-day lag and lead times is a manifestation of the well-known propagating nature of the MJO. Figure 7 shows the lagged correlations between the PCs of the two main modes (PC1 and PC2) for four different forecast lead times: 5, 7, 10 and 14 days. For the 5-day forecast the shape of the correlation coefficient appears very similar to observations in all three experiments (Fig. 7a), with a maximum when PC1 lags PC2 by two pentads. As the forecast lead time increases, the correlation coefficient decreases in all experiments compared to the 5-day forecast. For the 7-day forecast, the two modes are less correlated than for 5-day forecast, but the simulations still show vestiges of the eastward propagating nature. As the forecast lead time increases (~14-day), the lagged relationship vanishes in all experiments. However, in spite of the considerably lower correlation coefficients between the leading PCs than those found in observations, the DSST exhibits a better shape than either the CTRL or WSST cases suggesting that that higher temporal resolution SST forcing improves the simulation of the MJO's eastward propagation.

In order to study further the eastward propagation, the average wavenumber-frequency spectra of VP200 anomalies, including all forecasts lead times, are examined (Fig. 8). The spectra were computed by Fourier transforming latitudinal segments averaged between 10˚S and 10˚N for each year and at each forecast lead time, and then averaging over all 8 years and all forecast lead times from day 1 to day 30. In the figure, a positive zonal wavenumber refers to wave propagating eastward. The power in the observations is concentrated in the MJO timescales which is manifested as a broad peak located between 30 to 60 days and around wavenumber 1 (Fig. 8a). The spectral features in the three experiments are more similar to observations as the temporal resolution of the forcing SST increases (Fig. 8b-d). Although the magnitude is weaker than for the observations, the temporal and spatial scales of VP200 DSST MJO variability is in better agreement with observations than CTRL or WSST. The impact of the higher resolution forcing (DSST) extends clearly beyond day 10. In summary, the higher temporal resolution of SST forcing appears to play a definitive role in reproducing the characteristics of eastward propagating MJO closer to those that are observed.

c. Phase relationship

To investigate the change of convection-SST phase with increasing forecast lead time, we calculate the lagged correlation between filtered OLR and SST anomalies (Fig. 9). Strictly speaking, the SST anomalies are the daily surface temperature output from the model simulation. But, we refer to it as "SST" because the surface temperature data over the ocean is used in the calculations. Lagged correlation coefficients are computed between filtered SST anomalies and OLR anomalies for each 30-day forecast. Therefore, 184 30-day segments (8 year x 23 segment) are used for computing the lead-lag correlation coefficients each of which consists of 29 days (-14, …, + 14 day lag). Figure 9 shows the correlation coefficients as a function of forecast lead time averaged over the equatorial Indian Ocean (60-95E, 5S-5N). In the observations (Fig. 9a), the positive OLR anomalies (suppressed convection) lead enhanced SST and negative OLR (active convection) follow enhanced SST after several days. This is consistent with previous studies where the importance of ocean-atmosphere interaction on eastward propagating MJO has been well documented (e.g. Jones et al. 1998, Shinoda et al. 1998, Waliser et al. 1999, Woolnough et al. 2000, Wu et al. 2002, Matthews 2004, Rajendran and Kitoh 2006).

In the three experiments, the phase relationship between SST and convection becomes more similar to that in the observation as temporal resolution of SST increases (Fig. 9b-d). In WSST and DSST, the enhanced convection anomalies correctly lag the positive SST anomalies although the correlation is weaker than that observed. Convection lags SST by only few days, and shows an almost in-phase relationship through all forecast days. This results from the fact that the simulated MJO is the passive atmospheric response to the underlying SST anomalies, and the convective response in the model is too fast. Woolnough et al (2001) and Matthews (2004) reached similar conclusions.

In the DSST experiment, convection and SST show realistic phase relationship until about 4 days. This is due mainly to the direct influence of the prevailing phase relationship between atmospheric initial conditions and SST boundary conditions at the beginning of the forecast. However, as the forecast lead time increases, the relationship is adjusted by the model physics resulting in differences with observations. In the three atmospheric-only experiments, the MJO-related fluxes have no influence on the SST even if anomalies remain present. Therefore, the convection adjusts to a location where the SST is more favorable and results in nearly in-phase relationship between OLR and SST anomalies. However, in nature, as mentioned above, intraseasonal SST variations not only influence the atmosphere as a boundary forcing but, at the same time, they are influenced by atmospheric convection and circulation. Therefore, it is difficult to reproduce the observed phase relationship by using an atmosphere-only model. Such different phase relationship between MJO convection and SST is one of the main problems in atmosphere-only models due to the lack of coupling with the upper ocean.

d. Forecast Skill

To examine the potential forecast skill of the MJO, correlation coefficients between simulated and observed PC1 from filtered VP200 were computed for each forecast day (Fig. 10). The correlation coefficients are very similar among the different experiments for the first 8 days of the forecast. Although the forecast skill decreases as the lead time increases, the DSST shows the highest value after day 10. In DSST, the correlation coefficient is sometimes more than twice that of the CTRL after 10 days. As expected, the correlation in the WSST lies in the middle of the CTRL and DSST after day 10. Therefore, we can conclude that the higher temporal resolution in the boundary forcing is important not only for MJO simulation but also for MJO forecasting.

In order to examine the forecast spatial structure of MJO in the modeling results, composite analysis is performed for various forecast lead times. The composites are constructed based on the observed EOF PC1 using VP200 that was analyzed in previous section. In this manner, we can estimate collectively the forecast skill of each experiment by computing composites relative to observations. Composites for each lead and lag are produced using filtered VP200 relative to dates corresponding to local maxima of the observed PC1 greater than one standard deviation. These reference dates correspond to pentad 0. The threshold selected was determined to be high enough to capture the most representative MJO events and low enough to provide a statistically representative sample of all MJO events. Because of the discontinuous date from the end and beginning of the next year, the compositing was performed for each year and then averaged over each lead and lag day.

Figure 11 shows the time-longitude diagram of the composite MJO based on observations for various forecast lead times (5, 7, 12, and 14 days). At the beginning of forecast (day 5), the model integrations show a very similar eastward propagating pattern, similar to observations, in all three experiments. At forecast day 7, the amplitude has decreased universally with the propagating structure diminishing to the eastward of the date line. This reduction especially evident in the CTRL and the WSST is less so in the DSST experiment which still possess an obvious eastward propagation over the whole globe. However, the phase of convection shows a quadrature shift relative to observations. For example, in the reference pentad 0 at date line, a transition phase occurs in the observed fields while a maximum convection exists on the DSST. This phase shift can be explained by the SST-convection phase issue described in the previous section. At forecast day 12, the MJO signal in DSST still follows observations more closely than the other experiments with relatively strong amplitude and coherent structure. At day 14, although a wavenumber 1 structure is not as clear as it was before, there still remains a clear eastward propagating pattern in DSST with relatively strong amplitude. In the CTRL, the MJO structure appears as a stationary oscillation between the Indian Ocean and the western and central Pacific. The WSST has an eastward propagating signal that is clearer than CTRL but not as much so as in the DSST experiment.

We can conclude that the overall MJO structure is more predictable when the higher temporal resolution of SST is taken into account. In DSST, the simulations show stronger MJO with a more realistic propagating structure than found in the other experiments. However, the pattern correlations of the longitude-time diagrams between experiments and observation (Fig. 11) are similar for all experiments with low correlation coefficients because of the quarter cycle phase shift with respect to observations.

4. Summary and discussion

Previous studies (Fu et al. 2003, Inness and Slingo 2003, Fu and Wang 2004, Zheng et al. 2004, Rajendran and Kitoh 2006) have suggested a particular importance of the intraseasonal variability of SST on the simulation of the MJO. However, systematic biases in the mean SST state present in most coupled general circulation models limit the capability to the simulate the MJO. Based on the premise that the mean SST must be retained in models, we conducted three serial experiments using an AGCM and prescribed observed SST with increasing temporal resolution. Comparisons of the model's ability to simulate and predict MJO characteristics with monthly, weekly and daily averaged SSTs were made. The model forced with highest temporal SST showed a better intraseasonal signal than when forced with monthly and weekly averaged SST data. Three measures of the model's ability were considered; the MJO/ISO activity of 200 hPa velocity potential field over the entire Asian-monsoon region at all lead-times, the percentage of filtered variance by two leading EOF modes (and hence the eastward propagation of MJO), the power of the wavenumber one eastward propagating mode, and the forecast skill of MJO. Each of these metrics faired considerably better when the model was forced with daily SST. However, the phase relationship between convection and SST was not well simulated even in the DSST experiment.

The phase relation discrepancy between observations and atmosphere-only models is a well known problem. The different phase relationship resulting in atmospheric-only experiments is due to the fact that the convection responds to the underlying SST but the change of surface fluxes induced by the MJO itself, does not influence the prescribed SST. However, the coupled models produce a more realistic phase relationship compared to the atmosphere-only runs because the flux anomalies are allowed to modify the ocean (Fu et al. 2003, Fu and Wang 2004, Zheng et al. 2004, Rajendran and Kitoh 2006). Wu et al. (2002) examined the MJO response by 10 different atmospheric-only models forced with the same observed weekly SST. They showed that the intraseasonal variability is dominated by a “free (intraensemble)” component rather than a “forced” component which is in phase with the prescribed SST. Our results help to emphasize the importance of treating the MJO as a coupled phenomenon that is able to link directly the free variability with the underlying SST.

Figure 12 shows the results of the lag correlation for filtered precipitation and SST in long-term integration of the SNU AGCM and a fully coupled GCM (CGCM) over the winter (November through February) season. The CGCM is described in section 2. Both models are integrated for a 40 year period. The AGCM is run with prescribed monthly mean SSTs.

There is a considerable difference in the phase relationship between intraseasonally filtered precipitation and SSTs in both the AGCM and CGCM results. In contrast to the AGCM, the lag associated with the maximum correlation in the CGCM is about 5 days, indicating that the precipitation and SST anomalies are in quadrature, which is consistent with observations. Therefore, the ocean-atmosphere coupled process is crucial for a better simulation and prediction of the MJO/ISO. This issue is currently being examined with CGCM and AGCM using a similar experimental design to that used in this study. In order to keep the mean states close to each other in CGCM and AGCM, the SST outputs from the coupled run are be used as a boundary condition of AGCM.

Acknowledgements

This work is supported by the Korea Meteorological Administration Research and Development Program under Grant CATER_2006-4206 and the second stage of the Brain Korea 21 Project. The second and third authors are supported by Climate Dynamics Division of the United States National Sciences Foundation under Award NSF-ATM 0531771 and the Georgia Institute of Technology Foundation. Much of the work presented here was accomplished during a visit by Hye-Mi Kim to Georgia Institute of Technology in 2006.

References

Agudelo, P. A., J. A. Curry, C. D. Hoyos, and P. J. Webster, 2006: Transition Between Suppressed and Active Phases of Intraseasonal Oscillations in the Indo-Pacific Warm Pool. *J. Climate*, **19**, 5519-5530.

Agudelo, P.A., C.D. Hoyos, P.J. Webster and J.A. Curry, 2008: Understanding the poor simulation and prediction of intraseasonal variability by numerical models, *Clim Dyn.*, In Revision.

Bergman, J. W., H. H. Hendon, and K. M. Weickmann, 2001: Intraseasonal air-sea interactions at the onset of El Nino. *J. Climate*, **14**, 1702-1719.

Bonan, G. B., 1998: The land surface climatology of the NCAR land surface model coupled to the NCAR Community Climate Model. *J. Climate,* **11,** 1307–1326.

Chen. T. C., and J. C. Alpert, 1990: Systematic errors in the annual and intraseasonal variations of the planetary-scale divergent circulation in NMC medium-range forecasts. *Mon. Wea. Rev.,* **118**, 2607-2623.

Ferranti, L., T. N. Palmer, F. Molteni, and K. Klinker, 1990: Tropical-extratropical interaction associated with the 30-60 day oscillation and its impact on medium and extended range prediction*.* *J. Atmos. Sci*., **47**, 2177-2199.

Fu, X., B. Wang, T. Li, and J. P. McCreary, 2003: Coupling between northward propagation intraseasonal oscillations and sea surface temperature in the Indian Ocean. *J. Atmos. Sci.*, **60**, 1733-1753.

Fu, X., and B. Wang, 2004: Differences of boreal summer intraseasonal oscillations simulated in an atmosphere-ocean coupled model and an atmosphere-only model. *J. Climate*, **17**, 1263-1271.

Fu, X., B. Wang, D. E. Waliser, and L. Tao, 2007: Impact of atmosphere-ocean coupling on the predictability of monsoon intraseasonal oscillations. *J. Atmos. Sci.,* **64**, 157-174.

Hendon H. H., and M. L. Salby, 1994: The life cycle of the Madden–Julian oscillation. *J. Atmos. Sci*, **51**, 2225–2237.

Hendon, H. H., and J. Glick, 1997: Intraseasonal air-sea interaction in the tropical Indian and Pacific Oceans. *J. Climate*, **10**, 647-661.

Hendon, H. H., B. Liebemann, M. Newman, J. Glick, and J. E. Schemm, 2000: Medium-range forecast errors associated with active episodes of the Madden-Julian oscillation. *Mon. Wea. Rev.,* **128**, 69-86.

Holtslag, A. A. M., and B. A. Boville, 1993: Local versus nonlocal boundary layer diffusion in a global climate model. *J. Climate,* **6,** 1825–1842.

Hoyos, C. D., 2006: *Intraseasonal Variability: Processes, Predictability and Prospects for Prediction*. PhD Thesis, Georgia Institute of Technology, 188 pp. (http://hdl.handle.net/1853/10530)

Hoyos C. D., and P. J. Webster, 2007: The Role of Intraseasonal Variability in the Nature of Asian Monsoon Precipitation. *J. Climate*, 20 (17), 4402-4424

Inness, P. M., and J. M. Slingo 2003: Simulation of the Madden-Julian Oscillation in a coupled general circulation model. Part I: Comparisons with observations and an atmosphere-only GCM, *J. Climate*, 16, 345–364.

Inness, P. M., J. M. Slingo, E. Guilyardi, and J. Cole, 2003: Simulation of the Madden-Julian oscillation in a coupled general circulation model. Part II: The role of basic state. *J. Climate*, **16**, 365-382.

Jones, C., D. E. Waliser, and C. Gautier, 1998: The influence of the Madden-Julian oscillation on ocean surface heat fluxes and sea surface temperature. *J. Climate*, **11**, 1057-1072.

Jones, C., and J. E. Schemm, 2000: The influence of intraseasonal variations on medium-to extended-range weather forecasts over South America. *Mon. Wea. Rev.*, **128**, 486-494.

Jones, C., D. E. Waliser, W. K. Lau, and W. Stern, 2004: The Madden-Julian oscillation and its impact on Northern Hemisphere weather predictability. *Mon. Wea. Rev.*, **132**, 1462-1471.

Kanamitsu, M., W. Ebisuzaki, J. Woollen, S.-K. Yang, J. J. Hnilo, M. Fiorino, and G. L. Potter, 2002: NCEPDEO AMIP-II Reanalysis (R-2). *Bull. Amer. Meteor. Soc.,* **83,** 1631–1643.

Kang, I. S., S. I. An, C. H. Joung, S. C. Yoon, S. M. Lee, 1989: 30-60 day oscillation appearing in climatological variation of outgoing longwave radiation around East Asia during summer. *J. Korean Meteorol. Soc.*, **25,** 149-160.

Kang, I. S., C. H. Ho, and Y. K. Lim, 1999: Principal modes of climatological seasonal and intraseasonal variations of the Asian summer monsoon. *Mon. Wea. Rev.,* 127, 322-340.

Kang, I. S., and Coauthors, 2002: Intercomparison of the climatological seasonal variations of Asian summer monsoon precipitation simulated by 10 GCMs. *Climate Dyn*., **19**, 383-395.

Kemball-Cook, S. R., B. Wang, and X. Fu, 2002: Simulation of the intraseasonal oscillation in the ECHAM4 model: The impact of coupling with an ocean model. *J. Atmos. Sci.,* **59**, 1433-1453.

Kim, J. K., I. S. Kang, and C. H. Ho, 1998: East Asian summer monsoon simulated by the Seoul National University GCM. *Proc. International Conference on Monsoon and Hydrologic Cycle.* 227-231.

Kim, H. M., I. S. Kang, B. Wang, and J. Y. Lee, 2007: Interannual variations of the boreal summer intraseasonal variability predicted by ten atmosphere-ocean coupled models. *Climate Dyn*., doi: 10.1007/s00382-007-0292-3

Kug, J. S., I. S. Kang, and D. H. Choi, 2007: Seasonal climate predictability with tier-one and tier-two prediction systems. *Climate Dyn*., doi: 10.1007/s00382-007-0264-7

Lau, K. M., and P. H. Chan, 1986: Aspects of the 40-50 day oscillation during the Northern summer as inferred from outgoing longwave radiation. *Mon. Wea. Rev.,* **114**, 1354-1367.

Lau, K. M., and F. C. Chang, 1992: Tropical Oscillations and their Predictions in the

NMC Operational Forecast Model. *J. Climate*, **5**, 1365-1378.

Lawrence, D. M. and P. J. Webster, 2002: The boreal summer intraseasonal oscillation: Relationship between northward and eastward movement of convection. *J. Atmos. Sci.,* **59**, 1593-1606.

Lin, J. L., and Coauthors, 2005: Tropical intraseasonal variability in 14 IPCC AR4 climate models. Part I: Convective signals. *J. Climate*, **19**, 2665-2690.

Lo, F., and H. H. Hendon, 2000: Empirical prediction of the MJO. *Mon. Wea. Rev.*, **128**, 2528-2543.

Lorenc, A. C., 1984: The evolution of planetary scale 200 mb divergences during the FGGE year. *Quart. J. Roy. Meteor. Soc.*, **110**, 427-441.

Madden R. A., and P. R. Julian, 1994: Detection of a 40-50 day oscillation in the zonal wind in the tropical Pacific. *Mon. Wea. Rev*., **122**, 813-837.

Matthews, A. J., 2004: Atmospheric response to observed intraseasonal tropical sea surface temperature anomalies. *Geophys. Res. Lett.*, **31**, L14107, doi:10.1029/2004GL020474.

McFarlane, N. A., 1987: The effect of orographically excited gravity wave drag on the general circulation of the lower stratosphere and troposphere. *J. Atmos. Sci.,* **44,** 1775–1800.

Moorthi S., and M. J. Suarez, 1992: Relaxed Arakawa-Schubert: a parameterization of moist convection for general circulation models. *Mon. Wea. Rev.*, **120**, 978-1002.

Nakajima, T., and M. Tanaka, 1986: Matrix formulation for the transfer of solar radiation in a plane-parallel scattering atmosphere. *J. Quant. Spectrosc. Radiat. Transfer,* **35,** 13–21.

Noh, Y. and H. J. Kim, 1999: Simulations of temperature and turbulence structure of the oceanic boundary layer with the improved near- surface process. *J. Geophy. Res*, **104**, 15621–15634.

Rajendran, K., and A. Kitoh, 2006: Modulation of tropical intraseasonal oscillations by ocean-atmosphere coupling. *J. Climate*, **19**, 366-391.

Reichler, T., and J. O. Roads, 2005: Long-range predictability in the Tropics. Part II: 30-60 day variability. *J. Climate*, **18**, 634-650.

Reynolds, C., P. J. Webster, and E. Kalnay, 1994: Random error growth in the numerical prediction models. *Mon. Wea. Rev.*, **122**, 1281-1305.

Reynolds, R. W., N. A. Rayner, T. M. Smith, D. C. Stokes, and W. Wang, 2002: An improved in situ and satellite SST analysis for climate. *J. Climate,* **15,** 1609-1625.

Schemm, J. E., H. Van den Dool, and S. Saha, 1996: A multi-year DERF experiment at NCEP. Preprints, *11th Conf. on Numerical Weather Prediction*, Norfolk, VA, Amer. Meteor. Soc., 47-49.

Seo, K. H, J. K. E. Schemm, W. Wang, and A. Kumar, 2007: The boreal summer intraseasonal oscillation simulated in the NCEP Climate Forecast System: The effect of sea surface temperature. *Mon. Wea. Rev.*, **135**, 1807-1827.

Seo, K. H, J. K. E. Schemm, C. Jones, and S. Moorthi, 2005: Forecast skill of the tropical intraseasonal oscillation in the NCEP GFS dynamical extended range forecasts. *Climate Dyn*., doi: 10.1007/s00382-005-0035-2

Shinoda, T., H. H. Hendon, and J. Glick, 1998: Intraseasonal variability of surface fluxes and sea surface temperature in the tropical Western Pacific and Indian Ocean. *J. Climate*, **11**, 1685-1702.

Slingo, J. M., and Coauthors, 1996: Intraseasonal oscillations in 15 atmospheric general circulation models: Results from an AMIP diagnostic subproject. *Climate Dyn*., **12**, 325-357.

Sperber, K. R., S. Gualdi, S. Legutke, and V. Gayler, 2005: The Madden-Julian oscillation in ECHAM4 coupled and uncoupled general circulation models. *Climate Dyn*., **25**, 117-140.

Tracton, S., K. C. Mo, W. Chen, E. Kalnay, R. Kistler, and G. White, 1989: Dynamical extended range forecasting (DERF) at the National Meteorological Center. *Mon. Wea. Rev.,* **117,** 1604–1635.

Waliser, D. E., K. M. Lau, and J. H. Kim, 1999: The influence of coupled sea surface temperatures on the Madden-Julian Oscillation: A model perturbation experiment. *J. Atmos. Sci*., **56**, 333-358.

Waliser, D. E., and Coauthors, 2003: AGCM simulations of intraseasonal variability associated with the Asian summer monsoon. *Climate Dyn*., **21**, 423-446.

Wang, B., and X. S. Xie, 1998: Coupled modes of the warm pool climate system. Part I: The role of air-sea interaction in maintaining Madden-Julian Oscillation. *J. Climate*, **11,** 2116-2135.

Wang, B., P. J. Webster, H. Teng, 2005: Antecedents and self-induction of active-break south Asian monsoon unraveled by satellites. *Geophys. Res. Lett.*, **32**, L04704, doi:10.1029/2004GL020996.

Webster, P. J., T. Palmer, M. Yanai, R. Tomas, V. Magana, J. Shukla and A. Yasunari, 1998: Monsoons: Processes, Predictability and the prospects for prediction. *J. Geophys. Res*., 103 (TOGA special issue),14451-14,510.

Webster, P. J., E. F. Bradley, C. W. Fairall, J. S. Godfrey, P. Hacker, R. A. Houze Jr., R. Lukas, Y. Serra, J. M. Hummon, T. D. M. Lawrence, C. A. Russel, M. N. Ryan, K. Sahami, P. Zuidema,, 2002: The JASMINE pilot study. *Bull. Amer. Meteor. Soc.,* **83,** 1603-1629.

Webster, P. J., and C. Hoyos, 2004: Prediction of monsoon rainfall and river discharge on 15-30-day time scales. *Bull. Amer. Meteor.Soc.,* **85,** 1745-1765.

Woolnough, S. J., J. M. Slingo, and B. J. Hoskins, 2000: The relationship between convection and sea surface temperature on intraseasonal timescales. *J. Climate*, **13**, 2086-2104.

Woolnough, S. J., J. M. Slingo, and B. J. Hoskins, 2001: The organization of tropical convection by intraseasonal sea surface temperature anomalies. *Quart. J. Roy. Meteor. Soc*., **127**, 887-907.

Woolnough S. J., Vitart, F., Balmaseda M. A., 2007: The role of the ocean in the

Madden-Julian Oscillation: Implications for MJO prediction, *Quart. J. Roy. Meteor. Soc.,* 133 (622): 117-128 Part A

Wu, M. L. C., S. Schubert, I. S. Kang, and D. E. Waliser, 2002: Forced and free intraseasonal variability over the South Asian Monsoon region simulated by 10 AGCMs. *J. Climate*, **15**, 2862-2880.

Yasunari T., 1979: Cloudiness fluctuations associated with the Northern Hemisphere summer monsoon. *J. Met. Soc. Japan*, **57**, 227-242.

Zhang, C., 2005: Madden-Julian oscillation. *Rev. of Geophys*, **43**, RG2003, doi: 10.1029/2004RG000158.

Zheng, Y., D. E. Waliser, W. Stern, and C. Jones, 2004: The role of coupled sea surface temperatures in the simulation of the tropical intraseasonal oscillation. *J. Climate*, **17**, 4109-4134.

List of Figures

Figure 1. Variation of the prescribed surface temperature forcing (K) used in CTRL (control with monthly averaged SSTs: open circle), WSST (weekly averaged SSTs: x-mark), and DSST (daily SSTs: closed circle) experiments averaged over the Indian Ocean (60˚-90˚E, 10˚S-5˚N) for the period 15 Jan. 2004 to 13 Feb. 2004.

Figure 2. Schematic diagram of the climate DERF scheme. Each experiment consists of a series of 30-day forecasts that are initialized every 5 days. For example, a single forecast run starts on 6 Nov. 1998 and progresses for 30 days. The forecast is repeated starting on 11 Nov. 1998 for a further 30 day forecast, and so on, from 6 Nov. 1998 to 24 Feb. 1999. This procedure is repeated for the years 1999-2005.

Figure 3. Standard deviation of filtered VP200 (units: 10^{6} m^{2} s^{-1}) for (a) observations, (b) CTRL, (c) WSST, and (d) DSST for 10-day forecast.

Figure 4. Standard deviation of filtered VP200 averaged over 40˚-180˚E, 30˚S-30˚N (units: 10^{6} m^{2} s^{-1}) as a function of forecast day for CTRL (open circle), WSST (x-mark) and DSST (closed circle). The observed magnitude is about 3.4.

Figure 5. The first (left) and second (right) EOF of 30-day forecast for filtered VP200 from the observations, CTRL, WSST, and DSST, respectively.

Figure 6. Percentage of filtered variance accounted by the first two EOF modes of filtered VP200 as a function of forecast lead time for the CTRL (open circle), WSST (x-mark) and DSST (closed circle). The observed value is about 73%.

Figure 7. Lag correlation coefficients for observation (black), CTRL (blue), WSST (green), and DSST (red). Negative lags means PC2 leads PC1.

Figure 8. Wavenumber-frequency power spectra computed from equatorial (10˚S-10˚N) time-longitude for filtered VP200 averaged from 1-day to 30-day forecasts: (a) observations, (b) CTRL, (c) WSST, and (d) DSST. Variance units are 10^{12} m^4 s^{-2}.

Figure 9. Lag correlation coefficients between filtered OLR and SST anomalies over the region of 60˚E-95˚E, 5˚S-5˚N for a) observation, b) CTRL, c) WSST, and d) DSST as a function of forecast lead time. In observation, positive SST leads enhanced convection.

Figure 10. Correlation coefficients between predicted values and verifying values of PC1 for CTRL (open circle), WSST (x-mark) and DSST (closed circle). Correlations are shown as a function of forecast lead time.

Figure 11. Composite of VP200 anomaly (contour interval 10^6 m^2 s^{-1}) averaged along the equator (5˚S-5˚N) for observation and 5, 7, 12, and 14 day forecast.

Figure 12. Lag correlation coefficients between precipitation and SST anomalies over the region of 70˚E-90˚E, 5˚S-5˚N from AGCM (open circle) and CGCM (solid line). Negative lags indicate that SST leads variations in precipitation anomalies.

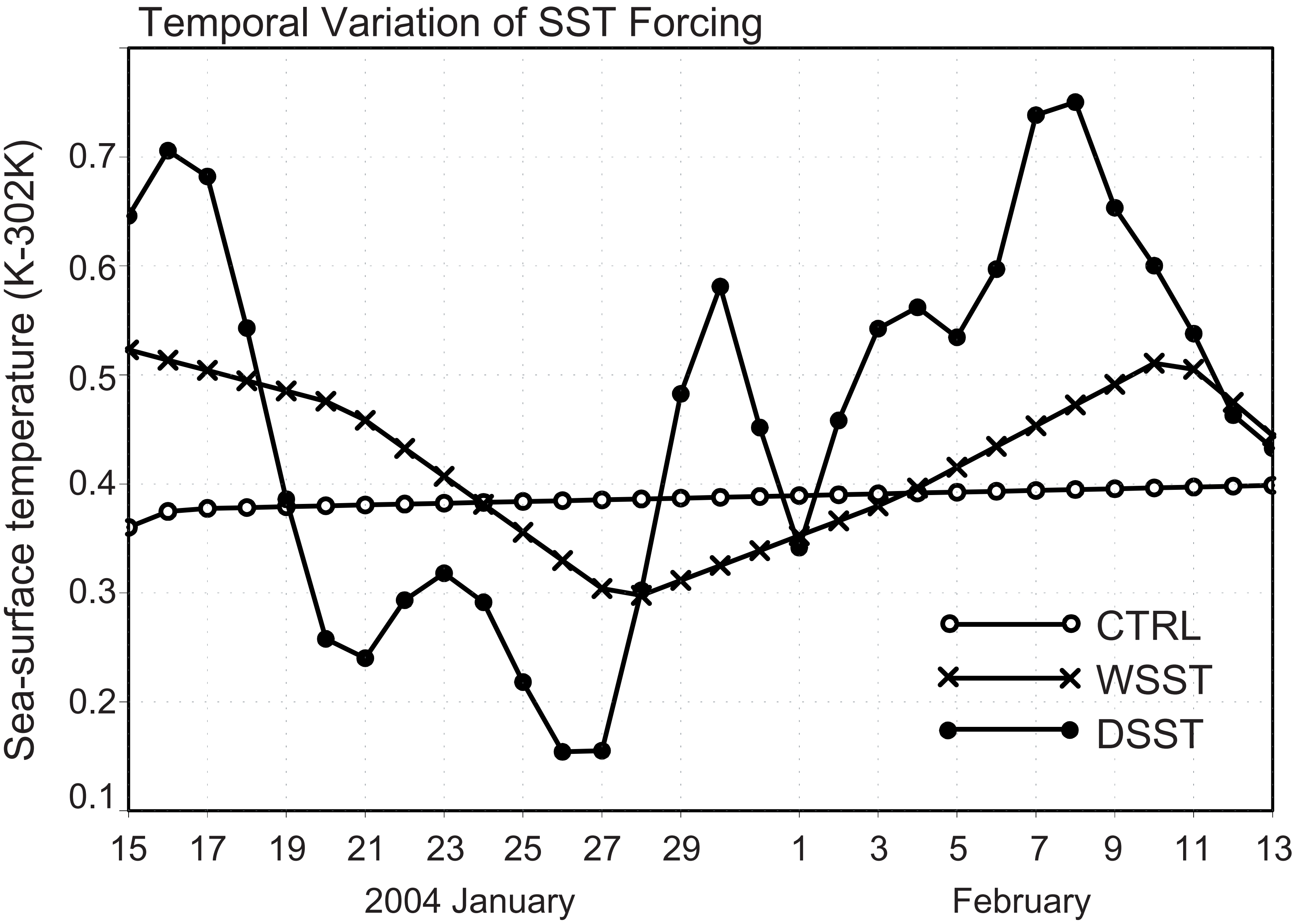

Figure 1. Variation of the prescribed surface temperature forcing (K) used in CTRL (control with monthly averaged SSTs: open circle), WSST (weekly averaged SSTs: x-mark), and DSST (daily SSTs: closed circle) experiments averaged over the Indian Ocean (60˚-90˚E, 10˚S-5˚N) for the period 15 Jan. 2004 to 13 Feb. 2004.

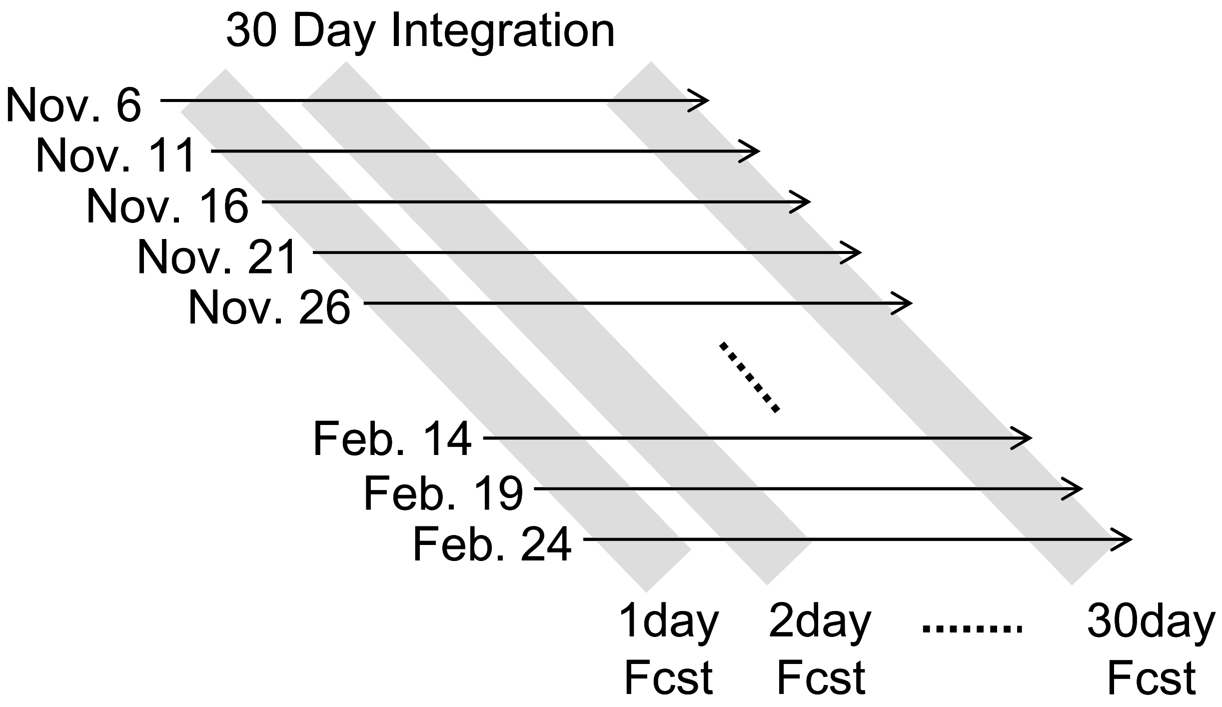

Figure 2. Schematic diagram of the climate DERF scheme. Each experiment consists of a series of 30-day forecasts that are initialized every 5 days. For example, a single forecast run starts on 6 Nov. 1998 and progresses for 30 days. The forecast is repeated starting on 11 Nov. 1998 for a further 30 day forecast, and so on, from 6 Nov. 1998 to 24 Feb. 1999. This procedure is repeated for the years 1999-2005.

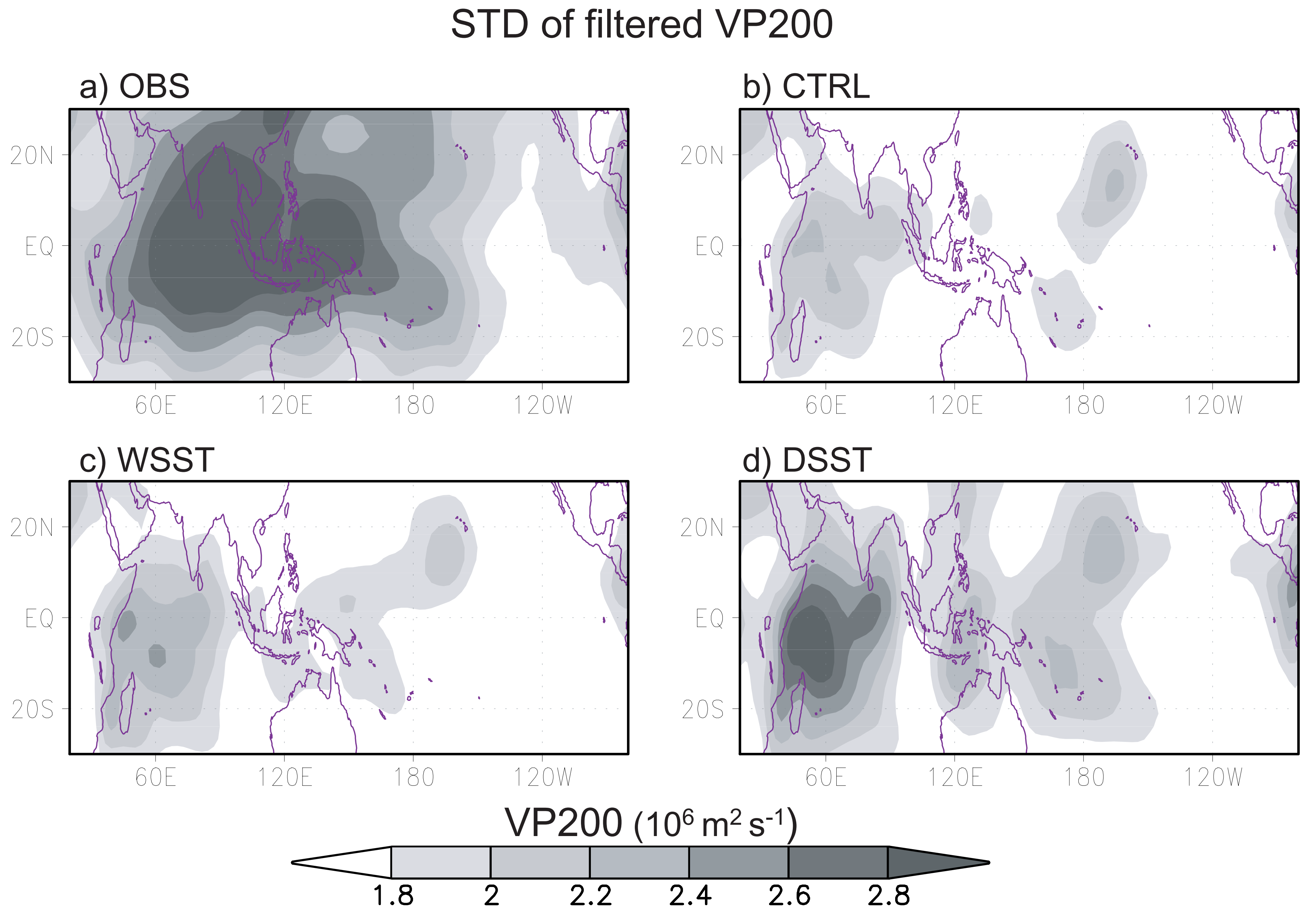

Figure 3. Standard deviation of filtered VP200 (units: 10^6 m^2 s^{-1}) for (a) observations, (b) CTRL, (c) WSST, and (d) DSST for 10-day forecast.

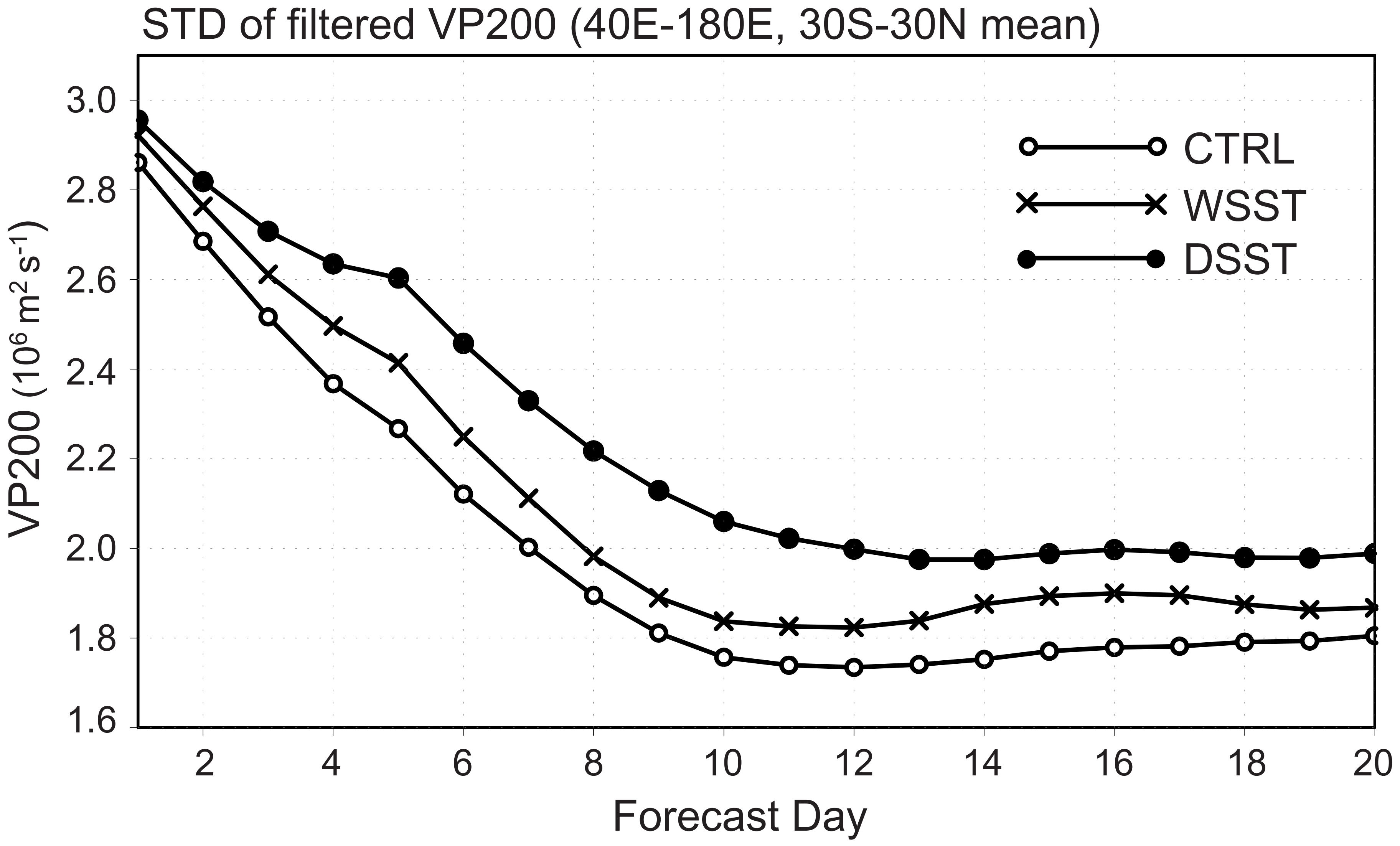

Figure 4. Standard deviation of filtered VP200 averaged over 40˚-180˚E, 30˚S-30˚N (units: 10^6 m^2 s^{-1}) as a function of forecast day for CTRL (open circle), WSST (x-mark) and DSST (closed circle). The observed magnitude is about 3.4.

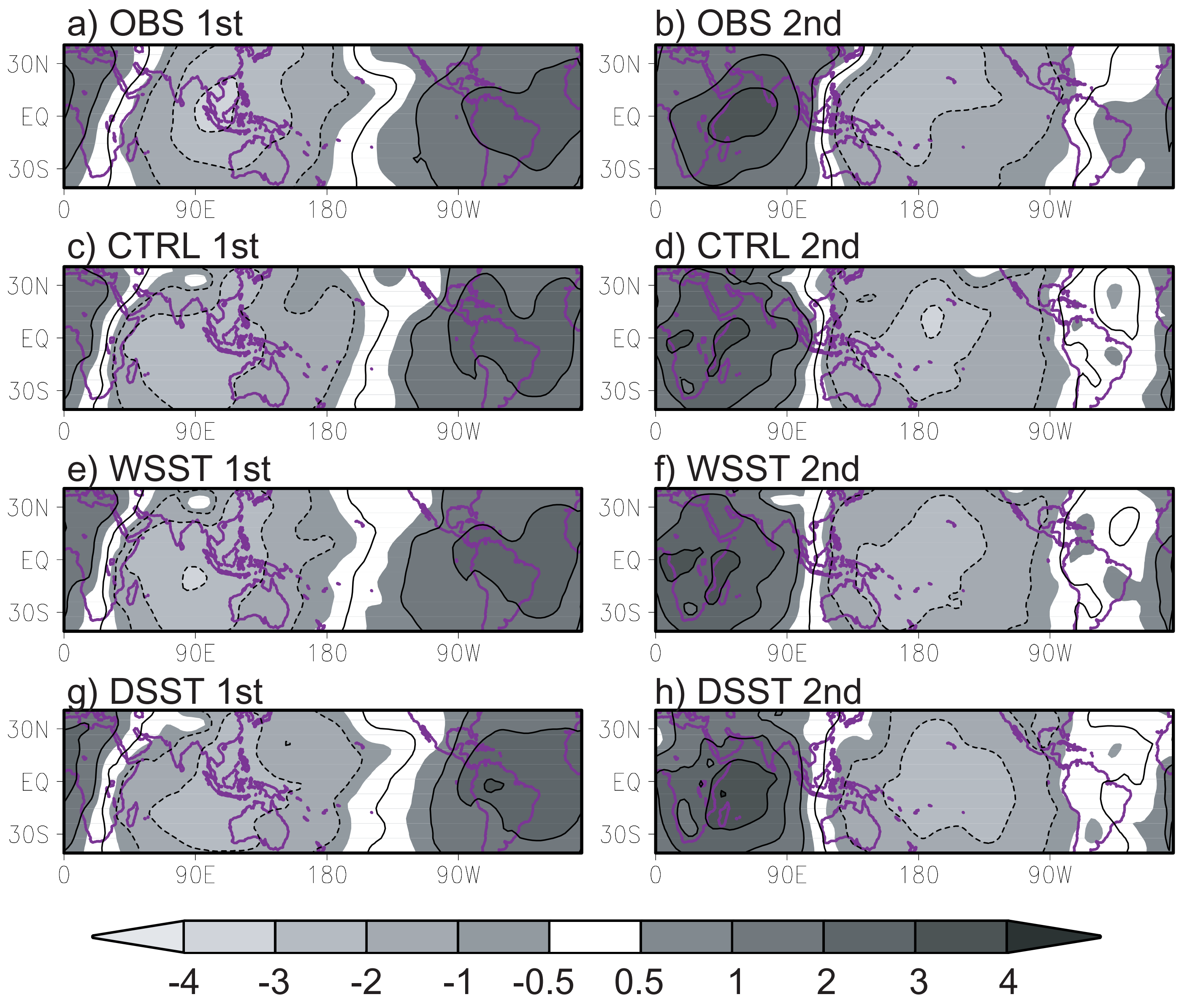

Figure 5. The first (left) and second (right) EOF of 30-day forecast for filtered VP200 from the observations, CTRL, WSST, and DSST, respectively.

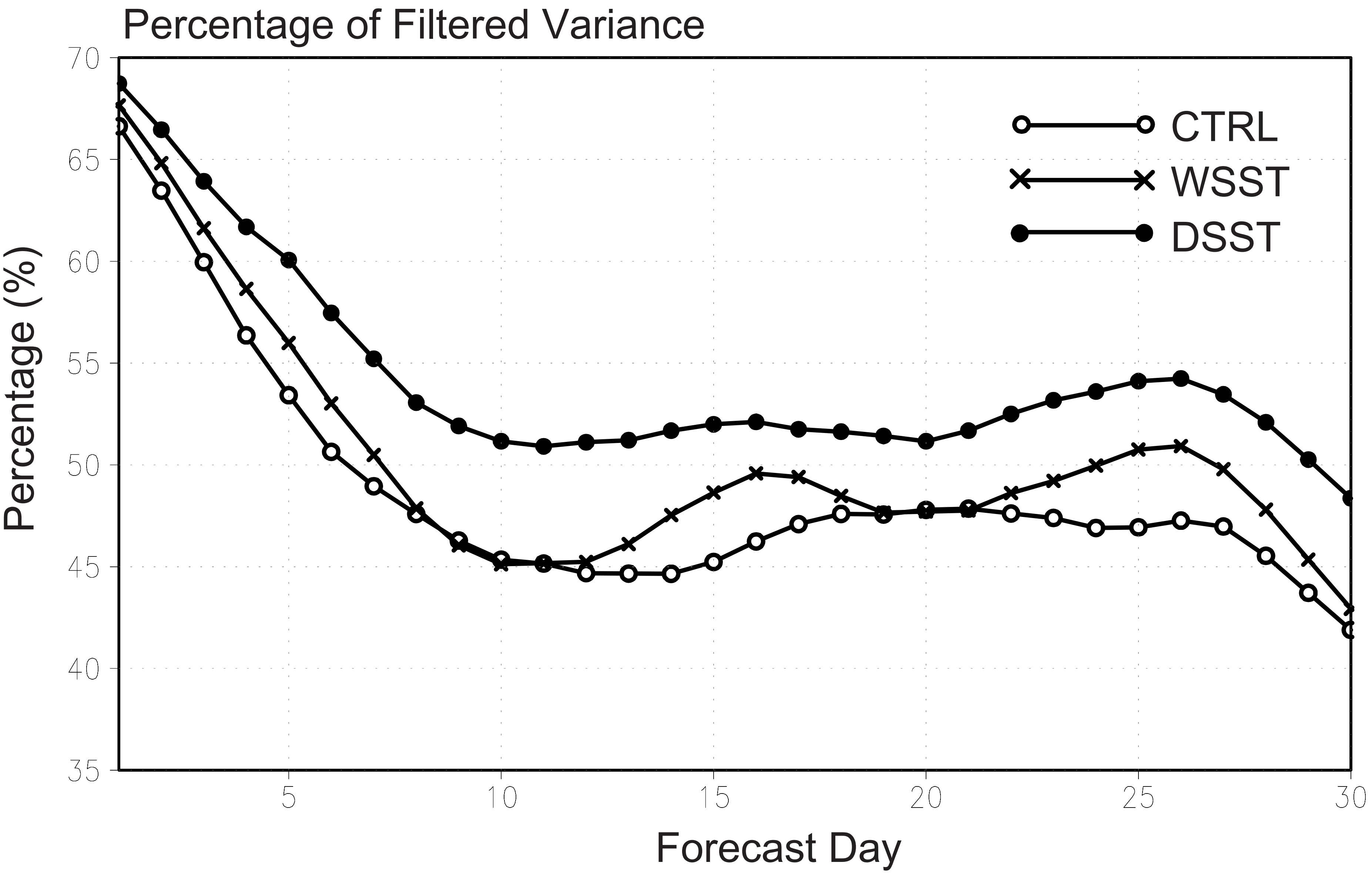

Figure 6. Percentage of filtered variance accounted by the first two EOF modes of filtered VP200 as a function of forecast lead time for the CTRL (open circle), WSST (x-mark) and DSST (closed circle). The observed value is about 73%.

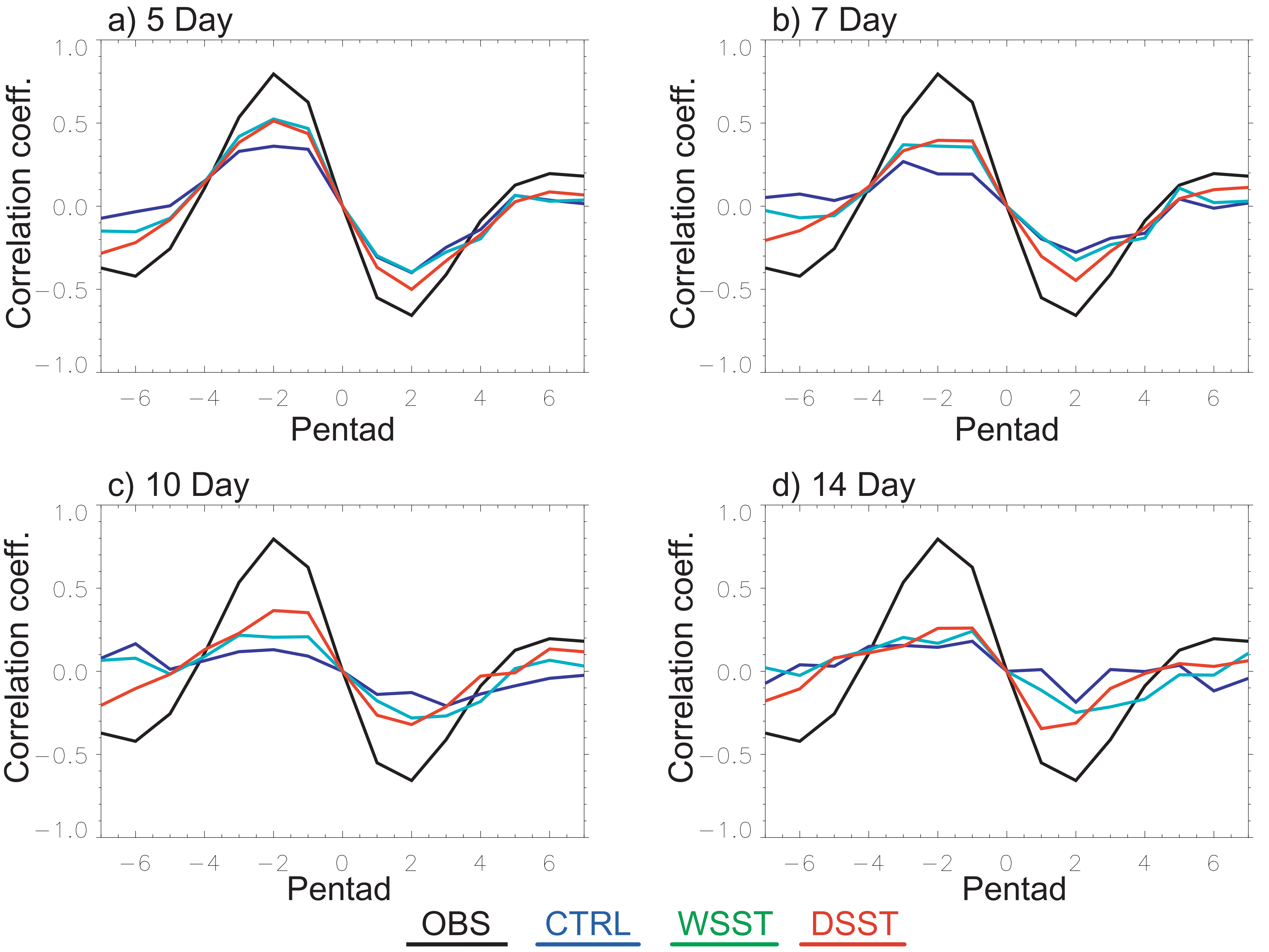

Figure 7.Lag correlation coefficients for observation (black), CTRL (blue), WSST (green), and DSST (red). Negative lags means PC2 leads PC1.

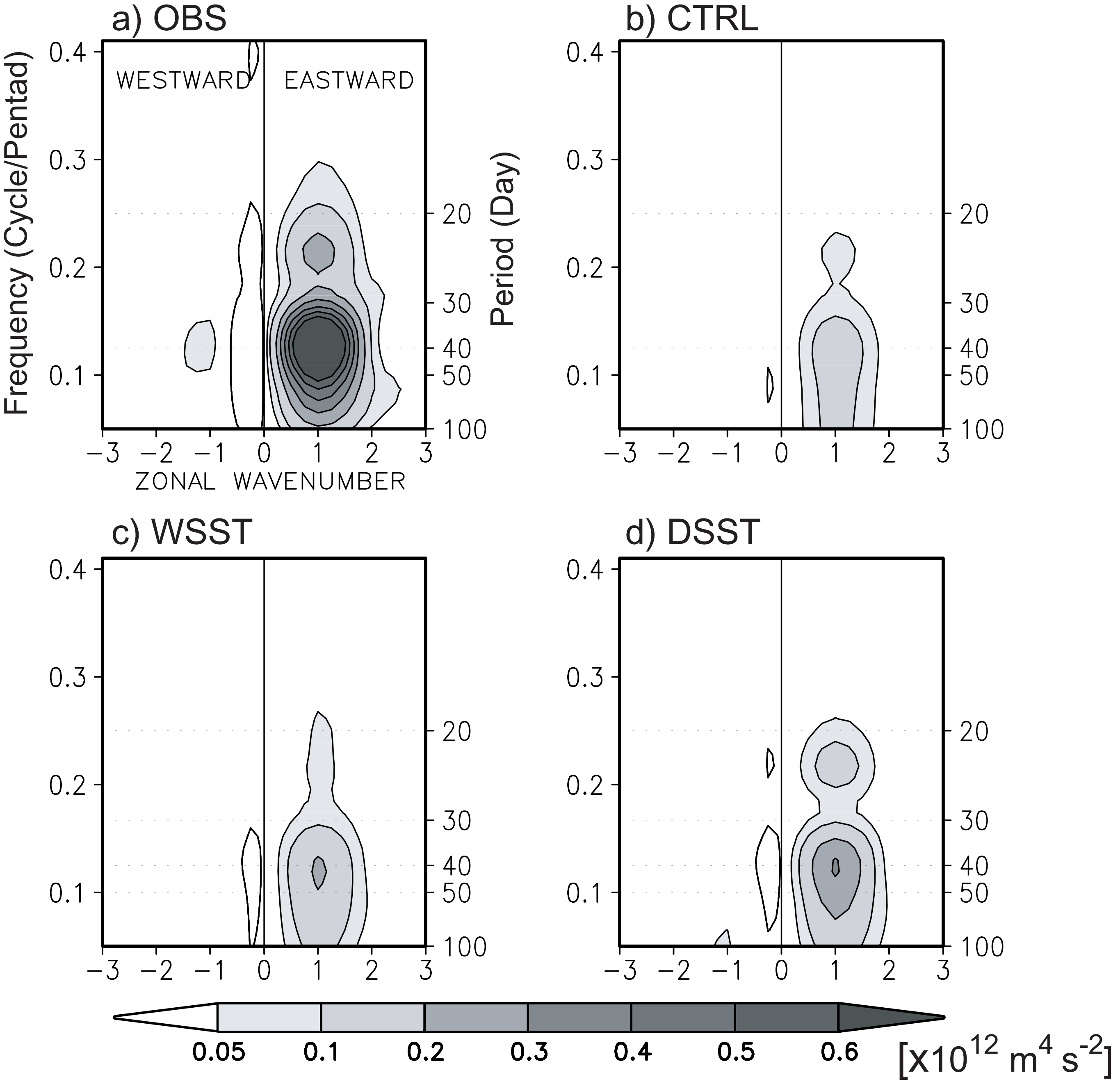

Figure 8. Wavenumber-frequency power spectra computed from equatorial (10˚S-10˚N) time-longitude for filtered VP200 averaged from 1-day to 30-day forecasts: (a) observations, (b) CTRL, (c) WSST, and (d) DSST. Variance units are 10^{12} m^4 s^{-2}.

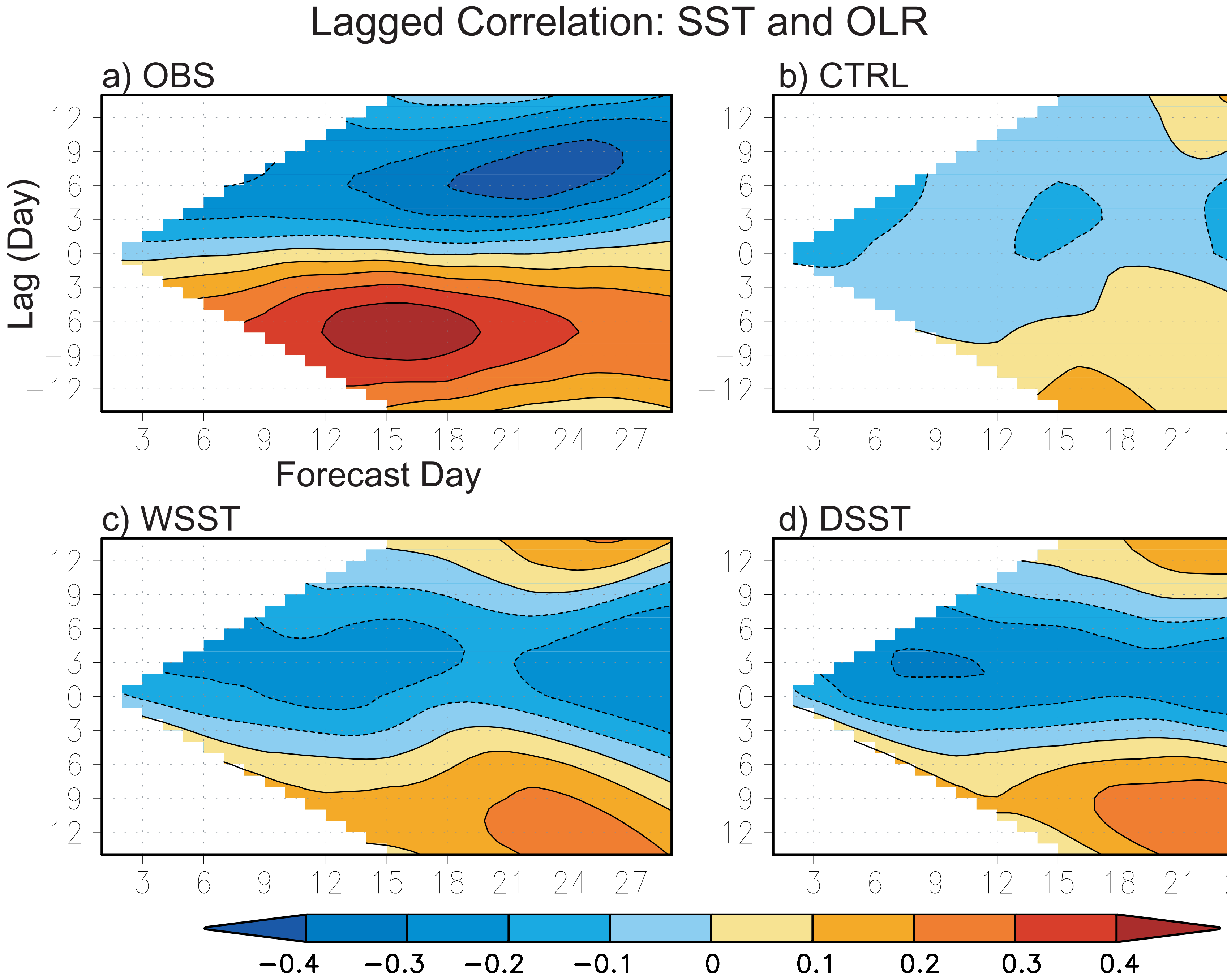

Figure 9. Lag correlation coefficients between filtered OLR and SST anomalies over the region of 60˚E-95˚E, 5˚S-5˚N for a) observation, b) CTRL, c) WSST, and d) DSST as a function of forecast lead time.
In observation, positive SST leads enhanced convection.

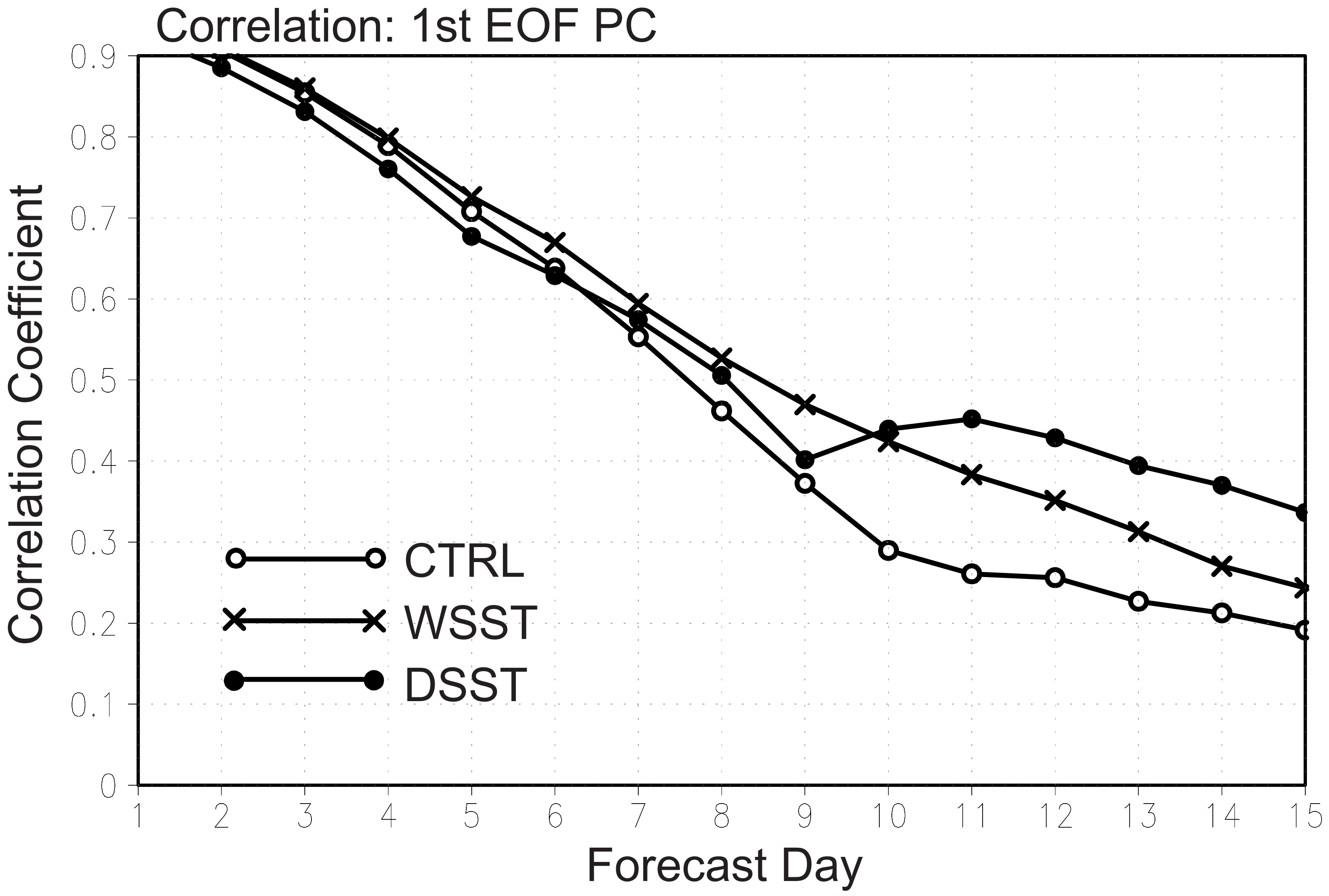

Figure 10. Correlation coefficients between predicted values and verifying values of PC1 for CTRL (open circle), WSST (x-mark) and DSST (closed circle). Correlations are shown as a function of forecast lead time.

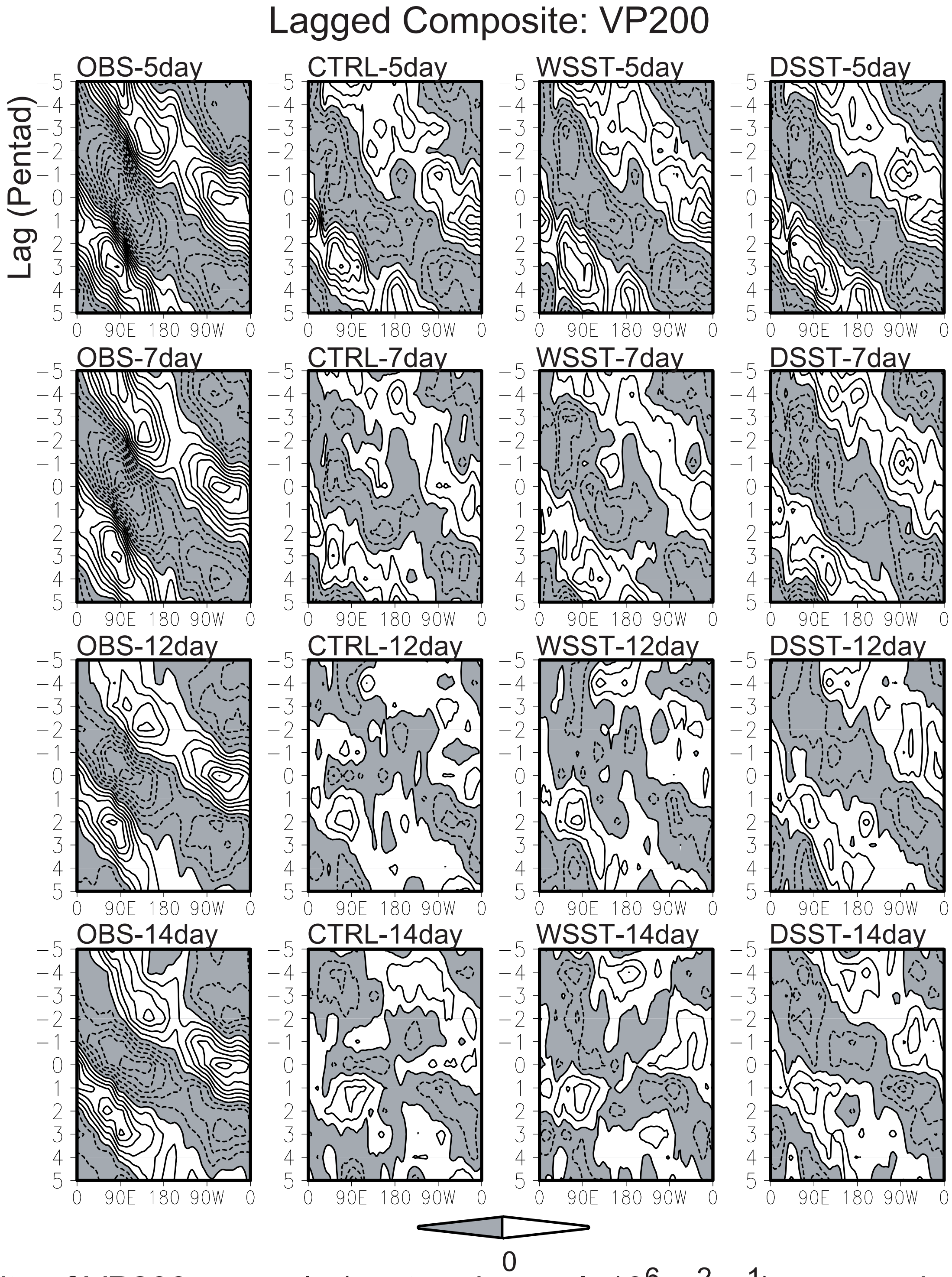

Figure 11. Composite of VP200 anomaly (contour interval: 10^6 m^2 s^{-1}) averaged along the equator (5˚S-5˚N) for observation and 5, 7, 12, and 14 day forecast.

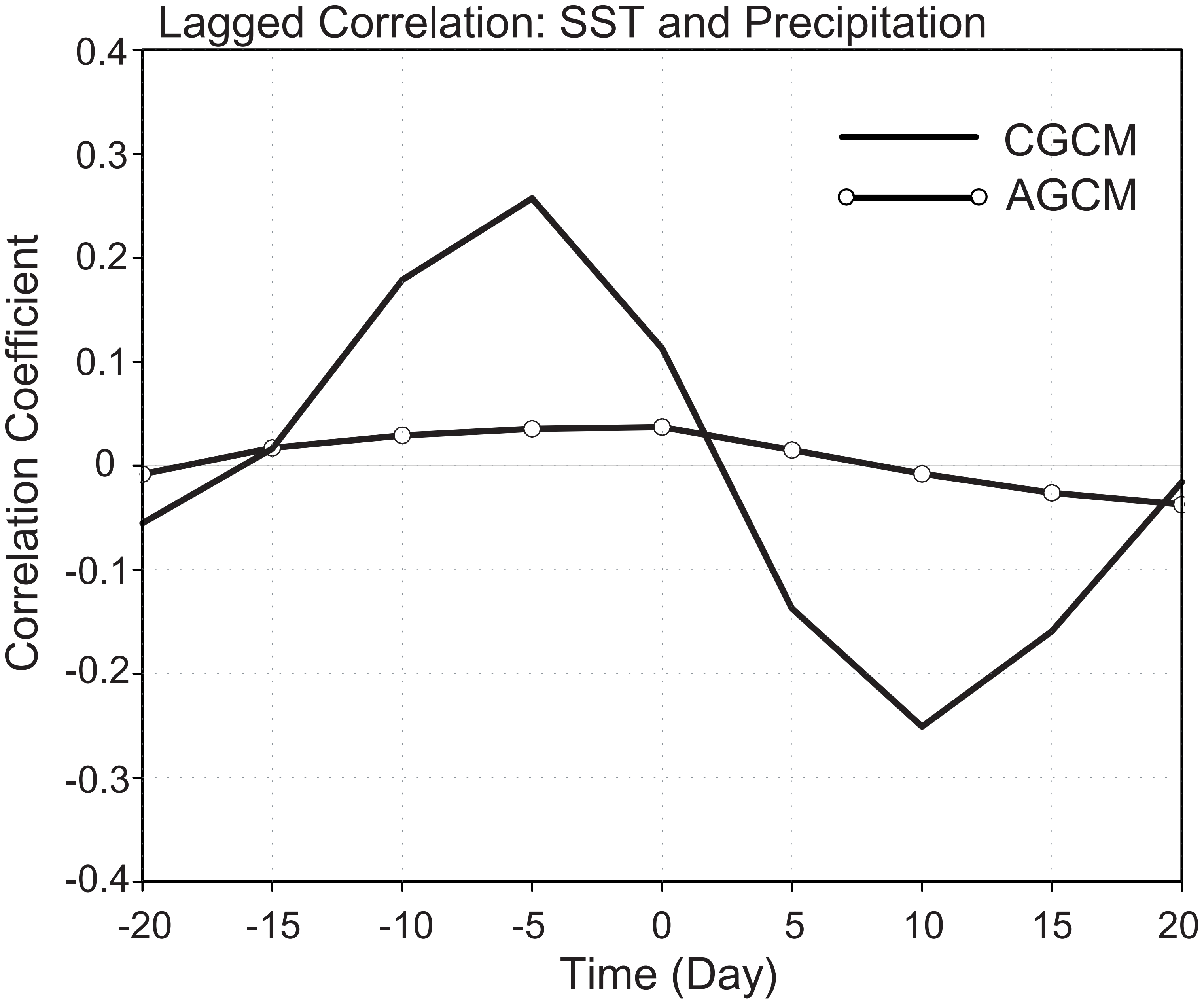

Figure 12. Lag correlation coefficients between precipitation and SST anomalies over the region of 70˚E-90˚E, 5˚S-5˚N from AGCM (open circle) and CGCM (solid line). Negative lags indicate that SST leads variations in precipitation anomalies.